3-D FDTD Design Analysis of a 2.4-GHz Polarization-Diversity Printed Dipole Antenna With Integrated Balun and Polarization-Switching Circuit for WLAN and Wireless Communication Applications

Huey-Ru Chuang, *Member, IEEE,* and Liang-Chen Kuo, *Student Member, IEEE*

***Abstract*—Detail numerical simulation, fabrication, and experimental measurement of a 2.4-GHz polarization-diversity printed dipole antenna are presented for wireless communication applications. Two orthogonal printed dipole antennas and each with a microstrip via-hole balun feeding structure are combined and fabricated on an FR-4 printed-circuit-board substrate. A p-i-n-diode circuit is used to switch and select the desired antenna polarization. In the antenna design simulation, a full-wave method of a three-dimensional finite-difference time-domain (FDTD) method is employed to analyze the entire structure of the printed antenna including the lumped elements of the polarization-selected p-i-n diode switching circuit. The Berenger perfectly matched layer absorbing-boundary condition is used for the FDTD computation. Numerical and measured results of antenna radiation characteristics, including input standing-wave ratio, radiation patterns, and polarization diversity are presented.**

***Index Terms*—2.4 GHz, finite difference time domain (FDTD), integrated balun, p-i-n diode, polarization diversity, printed dipole, switching circuit.**

I. Introduction

IN THE URBAN or indoor environments, the radio wave will propagate through complicated reflection or scattering processes. The polarization of the radio wave may change significantly. In order to effectively receive the communications signal, a polarization-diversity antenna for wireless communication applications, such as a wireless local area network (WLAN), may become an important requirement [1]–[4]. As shown in Fig. 1, a polarization-diversity antenna may have a pair of linearly polarized antennas and the polarization is selected by a switching circuit controlled by the baseband of the communicator for the best signal quality. A typical vertical-oriented dipole antenna basically radiates the vertically polarized wave and has an omnidirectional antenna pattern. In order to have a preferred planar antenna structure for the 2.4-GHz polarization-diversity antenna, a printed dipole antenna with a microstrip via-hole balun is designed. Research on printed dipole antennas with a microstrip-feedline incorporated with an $\lambda/4$ open-circuit stub has been reported, such as in [5]–[7]. It is known that a $\lambda/4$ open-stub transmission line can be equivalent to a shorted circuit and the open stub may radiate to cause the coupling effect and power losses. Hence, instead of an open stub, a via-hole through the substrate to the metal of bottom layer can be designed to be the via-hole balun structure.

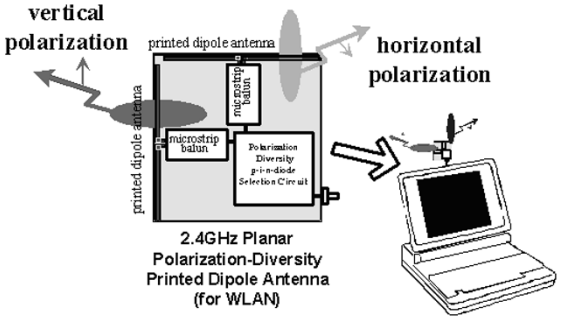

Fig. 1. Illustration of a 2.4-GHz polarization-diversity antenna, which consists of two orthogonal printed dipole antennas, integrated microstrip via-hole baluns, and a polarization-selection p-i-n-diodes circuit.

The design simulation of a complete polarization-diversity printed dipole structure includes the p-i-n diode switching and bias controlled circuit; in [8] a three-dimensional (3-D) finite-difference time-domain (FDTD) modeling of digital signal propagation in 3-D circuits with passive and active loads, which are assumed to be located in a free-space region. Hence, in this study, the FDTD modeling of an equivalent $R/L/C$ circuit model of the p-i-n diode and lumped elements of the polarization-switching circuit (of the antenna) soldered on the printed circuit board (PCB) substrate has to be derived. The Berenger perfectly matched layer (PML) absorbing-boundary condition (ABC) is used for the FDTD computation [9]. A 2.4-GHz printed dipole antenna and a polarization-diversity planar printed dipole antenna (with a polarization-selection

Manuscript received April 22, 2002. This work was supported by the National Science Council under Grant NSC 90-2213-E-006-055 and Grant NSC 91-2219-E-006-013.

The authors are with the Department of Electrical Engineering, National Cheng Kung University, Tainan, Taiwan, R.O.C. (e-mail: chuangh@eembox.ee.ncku.edu.tw).

Digital Object Identifier 10.1109/TMTT.2002.807838

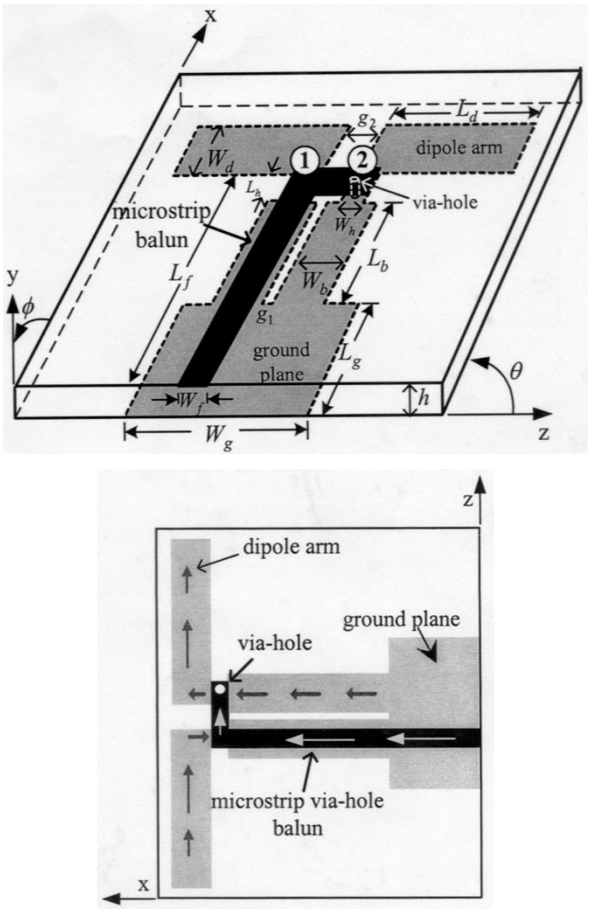

Fig. 2. Geometry of printed dipole antennas with integrated microstrip via-hole balun.

p-i-n-diodes circuit) have been realized by using the FR-4 PCB substrate. Measured radiation characteristics of the polarization-diversity planar dipole antenna, including input standing-wave ratio (SWR), radiation patterns, and polarization diversity with co-/cross-polarization level, are presented and compared with FDTD simulated results.

II. Printed Dipole Antenna With Via-Hole Balun

The geometry and photograph of realized 2.4-GHz planar printed dipole antennas are shown in Fig. 2. A microstrip via-hole balun acts as an unbalance-to-balance transformer from the feed coaxial line to the two printed dipole strips. The lengths of the dipole-arm strip and the microstrip balun are all approximately a quarter-wavelength. The ground plane of the microstrip line and the dipole strips are in the same plane. As indicated in this figure, a via-hole permits feed point 2 of a printed dipole strip to have the same phase as feed point 1 of the other printed dipole strip. Due to the 180° phase difference between the top strip and ground plane of the microstrip line, feed point 2 of the printed dipole strip will have 180° phase difference with the other feed point 1. Accurate dimensions of each part of the printed dipole and integrated via-hole balun needs to be numerically computed to achieve desired performance of the printed dipole antenna. The structure parameters of the printed dipole antenna with an open-stub or via-hole balun are listed as follows:

- *PCB substrate*: FR-4 (thickness $h = 1.6$ mm, $\varepsilon_r = 4.6$, $\tan\delta = 0.018$);
- *dipole arm*: length $L_d = 19$ mm, width $W_d = 6$ mm, gap $g_2 = 3$ mm;
- *microstrip balun*: length $L_f = 34$ mm, $L_b = 16$ mm, $L_h = 3$ mm, width $W_f = 3$ mm, $W_b = 5$ mm, $W_h = 3$ mm, gap $g_1 = 1$ mm;
- *via-hole*: radius $r = 0.375$ mm;
- *ground plane*: length $L_g = 10$ mm, width $W_g = 15$ mm.

The frequency range of interest for 2.4-GHz wireless communication systems is from 2.4 to 2.483 GHz. A higher frequency range to 3 GHz is chosen to observe the comparison between FDTD computation and measurement. In order to ensure the accuracy of the computed results, here, the FDTD cell size ($dx = dz = 0.25$ mm, $dy = 0.2$ mm) is smaller than a 1/20 wavelength of 3 GHz. The computation volume is $(150dx \times 60dy \times 180dz)$. Since the PML ABC requires a large amount of memory and an excessive CPU time, the choice of the parameters of PML ABC is very important. An eight-layer PML ABC and a reflection coefficient of 10^{-6} are used to realize reflectionless of all transmission waves between memory requirement and performance of the PML ABC.

To obtain multiple frequencies with only one FDTD run, a Gaussian pulse is selected by specifying the vertical direction of an y-directed excitation source within the coordinates $(i_s dx, j_s dy, k_s dz)$ of the source location at time step ndt as follows:

$$E^n_{in,\,y}(i_s, j_s, k_s) = E_o \exp\left[-\frac{(ndt - t_0)^2}{T^2}\right]. \qquad (1)$$

The time discrete step used is $dt = 0.441$ ps. The time delay t_0 is set to be $4T$. The Gaussian half-width T is determined by the pulsewidth and chosen to be approximate $20dx$. $2T$ was further defined as the width between the two symmetric points, which have 5% $(= e^{-3})$ of the maximum value of the pulse [10]. Thus, we get $T = 10dx/\sqrt{3}v = 8.379$ ps. Here, v is the velocity of the pulse in the substrate medium. Its Fourier transform is still of Gaussian shape. The performed simulation data tell us that the Gaussian pulse is enough long for 3000 time steps.

The cross section of the cylindrical via-hole is shown in Fig. 2. The hole size of the via is 0.375 mm in radius. To characterize the cylindrical via-hole in FDTD computation, a stair step or locally conformed FDTD method [11], [12] can be applied, although numerical results of these two methods have been compared and good agreement has been achieved since the via-hole is small. For the accuracy of computation, the locally conformed FDTD is adopted for the following computation. As shown in Fig. 3, the irregular magnetic-field components around the perfect electric conductor (PEC) cylindrical via-hole can be calculated by applying the contour integral formulation of Faraday's law. Note that the tangential electric-field and normal magnetic-field components are set to zero on the metallic surface of the cylindrical via-hole. Hence, the circumferential magnetic fields for the PEC cylindrical via-hole can be found in [11].

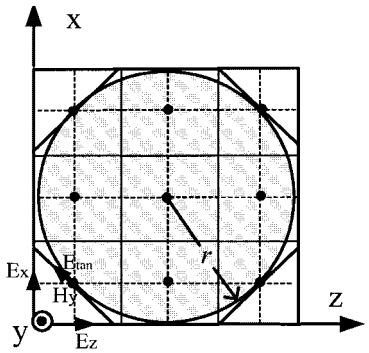

Fig. 3. Illustration of the cross-sectional view of the FDTD model for the cylindrical via-hole.

By using the transient data obtained from FDTD running, the time-domain to frequency-domain (TD–FD) transformation can get the electromagnetic fields of the antenna in the spectral domain. The surface current distribution on the metal plates can then be obtained directly from the tangential magnetic fields at a specific frequency. The complete far-field radiation pattern or response at a specific frequency can be determined by the near-to-far-field transformation method [13] that uses the near-field data obtained by post-processing stored FDTD running. Firstly, the tangential electric- and magnetic-field components on a total of six virtual planes surrounding the antenna element were converted to equivalent electric- and magnetic-current sources on the surface and, secondly, from the time-averaged Poynting vector of the scattered field expressed as follows [13]:

$$P_{\text{scat}} = \frac{1}{2}\,\text{Re}\left(E_\theta H_\phi^*\right) + \frac{1}{2}\,\text{Re}\left(-E_\phi H_\theta^*\right) = \frac{k^2}{32\pi^2\eta_o r^2}\left(\left|L_\phi + \eta_o N_\theta\right|^2 + \left|L_\theta - \eta_o N_\phi\right|^2\right) \quad (2)$$

where

$$E_\theta \cong -j\omega\left(A_\theta + \eta_o F_\phi\right) = -\frac{jke^{-jkr}}{4\pi r}\left(L_\phi + \eta_o N_\theta\right) \quad (3a)$$

$$E_\phi \cong -j\omega\left(A_\phi - \eta_o F_\theta\right) = +\frac{jke^{-jkr}}{4\pi r}\left(L_\theta - \eta_o N_\phi\right) \quad (3b)$$

with the vector phasors $\vec{N}$ and $\vec{L}$

$$N_\theta = \iint_s \left(J_x\cos\theta\cos\phi + J_y\cos\theta\sin\phi - J_z\sin\theta\right) \cdot e^{+jkr'\cos\psi}\,ds' \quad (4a)$$

$$N_\phi = \iint_s \left(-J_x\sin\phi + J_y\cos\phi\right) e^{+jkr'\cos\psi}\,ds' \quad (4b)$$

$$L_\theta = \iint_s \left(M_x\cos\theta\cos\phi + M_y\cos\theta\sin\phi - M_z\sin\theta\right) \cdot e^{+jkr'\cos\psi}\,ds' \quad (4c)$$

$$L_\phi = \iint_s \left(-M_x\sin\phi + M_y\cos\phi\right) e^{+jkr'\cos\psi}\,ds' \quad (4d)$$

and the equivalent phasor electric and magnetic current $\vec{J}_s$ and $\vec{M}_s$ are converted from the surface E- and H-fields.

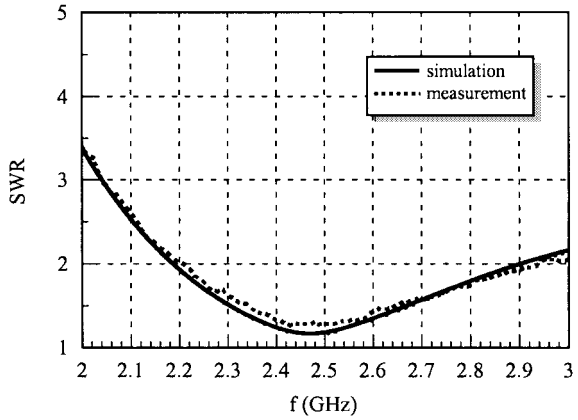

Fig. 4. FDTD simulation and measurement of VSWR of a 2.4-GHz printed dipole antenna with an integrated via-hole balun.

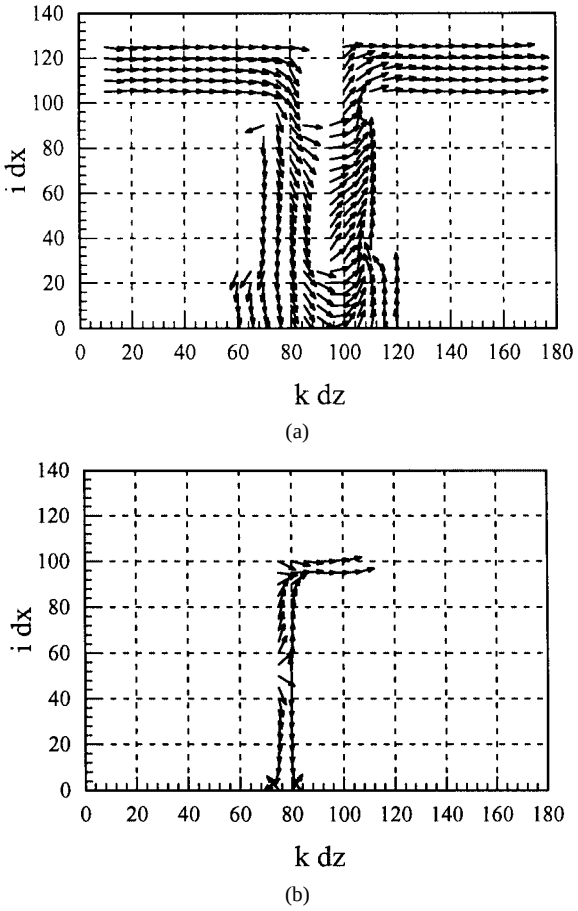

Fig. 5. Computed surface current density vectors on the top and bottom metal plates of a printed dipole antenna with a via-hole structure at 2.45 GHz.

The far-field radiation in spherical coordinates at any angular direction in free space can then be obtained.

Fig. 4 shows the computed and measured input voltage standing-wave ratio (VSWR) with good agreement. The VSWR of the printed dipole antenna with a via-hole balun is approximately lower than two from 2.2 to 2.9 GHz, with a bandwidth of approximately 28% (for SWR<2). Fig. 5 shows the computed surface current density vectors on the top and bottom metal plates. The directions of the surface current density vectors also show the balanced current distribution and

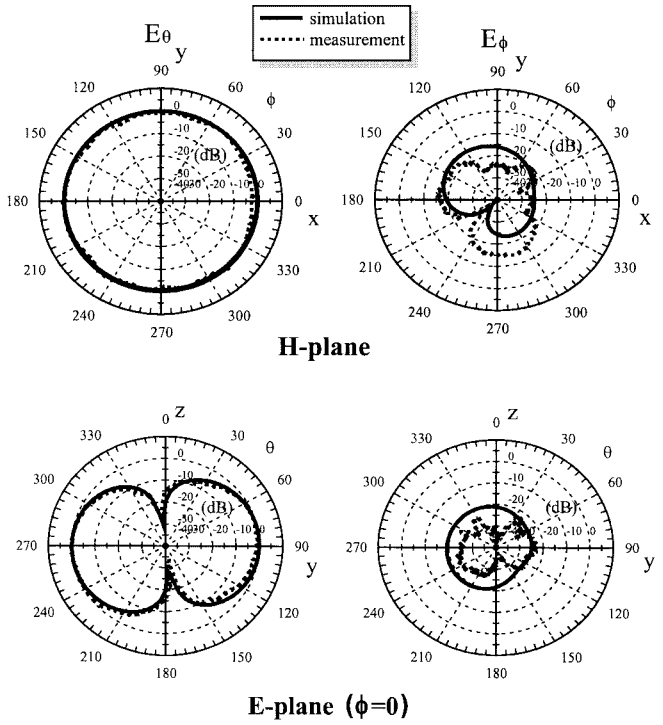

Fig. 6. FDTD simulation and measurement of radiation patterns of a printed dipole antenna with integrated via-hole balun at 2.45 GHz.

the 180° phase difference of the flowing current vectors at the two feed points of the printed dipole. This shows the function working of the integrated microstrip balun. Fig. 6 shows the computed and measured E- and H-plane antenna patterns. The H-plane pattern is quite omnidirectional and the E-plane pattern is also very close to that of an ideal dipole antenna. It can also be seen that the level of the cross-polarization field (E_ϕ) is less than -15 dB. The antenna directivity of the printed dipole is approximately 2.1 dBi.

III. Polarization-Diversity Printed Dipole Antenna

The geometry and photographs of a realized 2.4-GHz planar polarization-diversity antenna consists of two orthogonal printed dipole antennas and a p-i-n diode polarization-switching circuit are shown in Fig. 7. The dimension of each printed dipole is the same as the single dipole indicated in Section II. The dimension of the ground plane (of the switching circuit) is $L_t = 35$ mm and $W_t = 30$ mm. Each printed dipole has a microstrip via-hole balun. The terminals of the two baluns is connected to a p-i-n-diode selection circuit. The dc voltage $+5$ and -5 V from the bias circuit, fed through the cable to the input of the p-i-n-diode circuit section, will have controlled an OFF- or ON-state circuit of the p-i-n diode. The equivalent $R/L/C$ circuit models of a p-i-n diode containing packaged parasitic effects can be extracted from the measured S-parameters. The p-i-n diodes are with self-protect resistors of forward-biased current, RF choke inductors, and dc block capacitors to isolate the dc bias from the RF signal. The dc block capacitors should have a very low impedance at the RF frequency, while the RF choke inductors should have a very

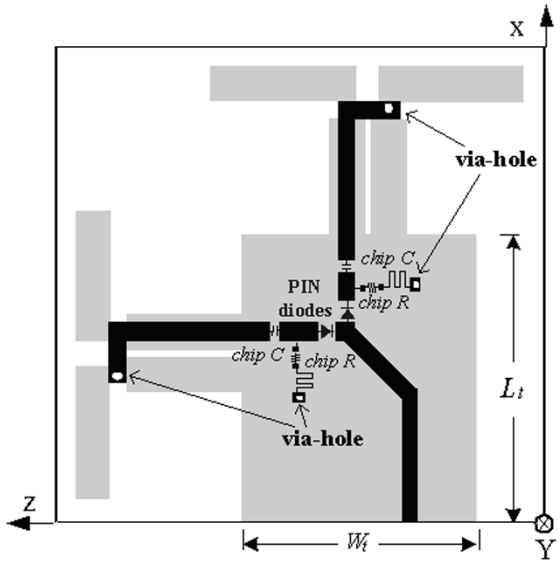

Fig. 7. Structure layout of a 2.4-GHz planar polarization-diversity antenna with a polarization-selection p-i-n diode circuit on an FR-4 PCB substrate. The size ($L \times W \times H$) of the p-i-n diode is $1 \times 3 \times 1$ mm, the chip resistor is $0.8 \times 1 \times 0.5$ mm and the chip capacitor is $1 \times 1.5 \times 0.5$ mm.

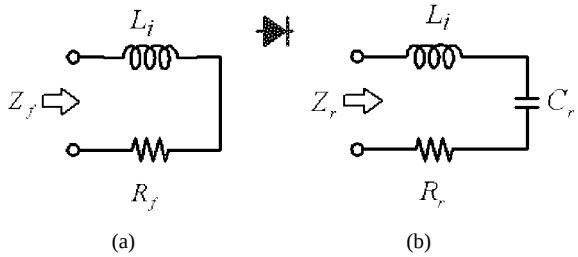

Fig. 8. Equivalent circuits for the ON and OFF states of a p-i-n diode. (a) Forward-bias (ON) state. (b) Reverse-bias (OFF) state [14].

high RF impedance. A quarter-wavelength meander line can be on the PCB substrate to replace the RF choke inductors.

The equivalent $R/L/C$ circuit parameters of the p-i-n diode (HSMP-389B), as shown in Fig. 8, are extracted from the measured S-parameters [14] as follows.

- At forward bias, the equivalent circuit is in series of $R_f = 0.8\ \Omega$ and $L_i = 1.7$ nH.
- At reverse bias, the equivalent circuit is in series of $R_r = 17.2\ \Omega$, $L_i = 1.7$ nH, and $C_r = 0.48$ pF.

Since the maximum forward-bias current of the p-i-n diode (HSMP-389B) is $I_F = 10$ mA (with a forward voltage $V_F = 0.7$ V), a self-protect resistor $R = 470\ \Omega$ should be added for the forward-bias 5 V. A dc block capacitors with $C = 75$ pF to have a very low impedance at the RF frequency is chosen. The size $(L \times W \times H)$ of the p-i-n diode is $1 \times 3 \times 1$ mm, the chip resistor is $0.8 \times 1 \times 0.5$ mm, and the chip capacitor is $1 \times 1.5 \times 0.5$ mm.

For FDTD modeling of the lumped elements, diode, and bipolar junction transistor, Melinda *et al.* [8] assume that all circuit components are located in a free-space region for convenience. Here, the p-i-n diode (with equivalent $R/L/C$ in the forward or reverse state) and other R/C components of the polarization-switching circuit are soldered on the PCB substrate. The FDTD modeling procedures that include the substrate

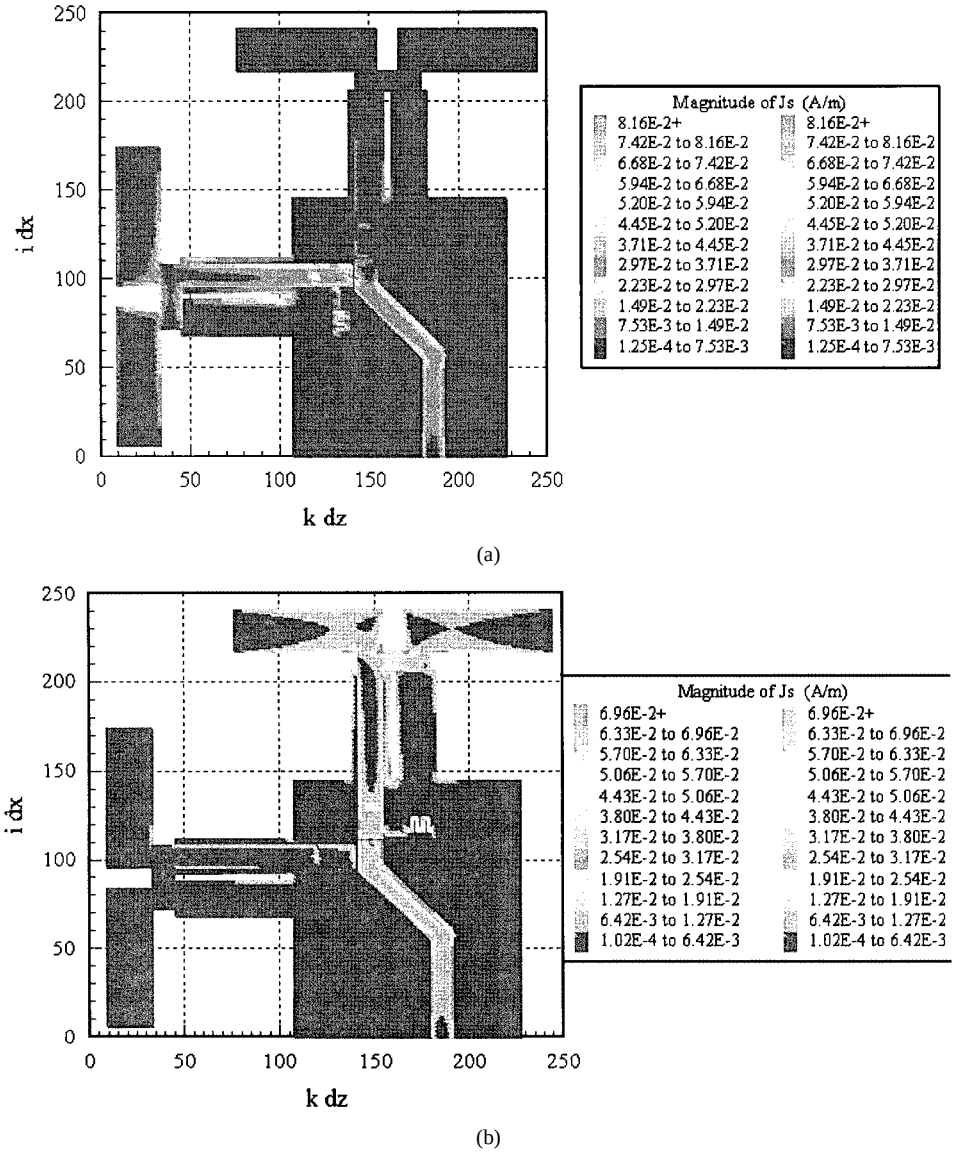

Fig. 9. Computed surface current density distribution of a polarization-diversity printed dipole antenna with: (a) vertical dipole selection and (b) horizontal dipole selection at 2.45 GHz.

parameters and electric conduction current on the substrate have to be established completely. For the FDTD modeling of the lumped elements located on the interface between the air and PCB substrate region, an average formulation of σ and ε is derived [10] and used in the following equations. Therefore, an assumed z-directed electric field of resistor, inductor, and capacitor models at a time-stepping $n+1$ algorithm can be expressed as (5)–(7), respectively, as shown at the bottom of page 380, where R is the value of the resistance, L is the value of the inductance, and C is the value of the capacitance.

Fig. 9 shows the magnitude of the computed surface current density distribution on the top and bottom metal plates of the polarization-diversity antenna for the selection of a vertical or horizontal dipole, respectively, at 2.45 GHz. It can be observed that the input RF signal is guided toward the vertical or horizontal dipole through the switched-ON p-i-n diode circuit path and microstrip balun. Only very little RF signal is coupled to the nonselected dipole path. From the phase distribution of the computed surface current, it is also found that the phase distributions of the surface current on the two dipole arms (of the selected vertical or horizontal dipole) are quite balanced. The phase of

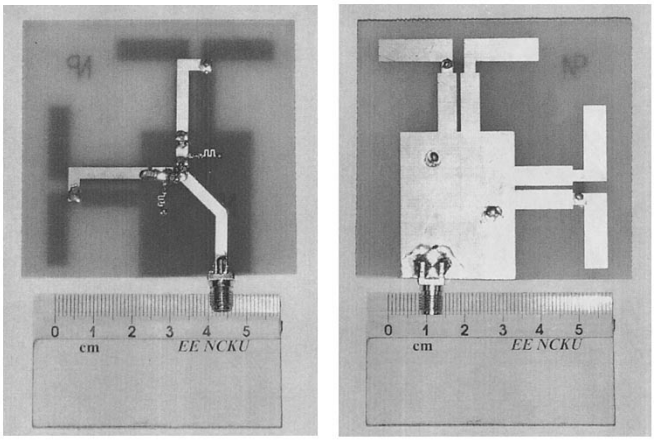

Fig. 10. Photographs of a realized 2.4-GHz planar polarization-diversity antenna on a FR-4 substrate with a polarization-switched p-i-n diode circuit.

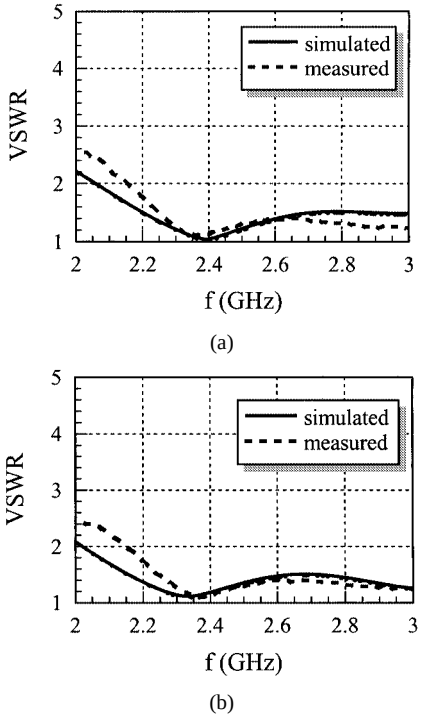

Fig. 11. Input VSWR of 2.4-GHz polarization-diversity printed dipole antenna. (a) Vertical dipole selection. (b) Horizontal dipole selection.

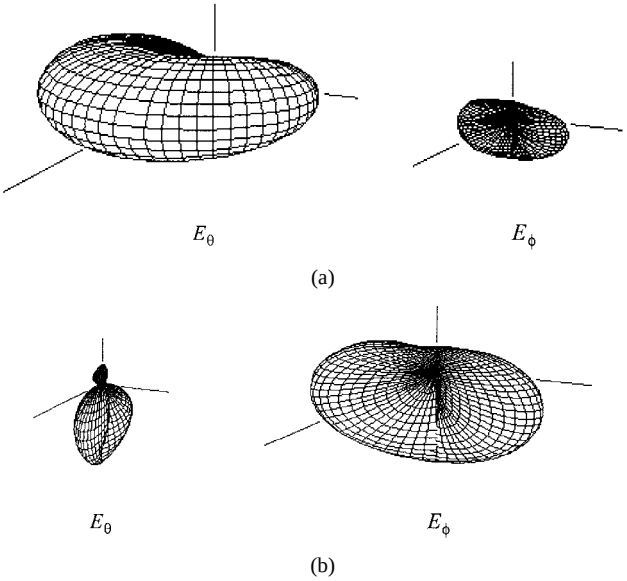

Fig. 12. Computed 3-D E_θ (vertical polarization) and E_ϕ (horizontal polarization) radiation patterns of a 2.4-GHz polarization-diversity printed dipole antenna. (a) Vertical dipole selection. (b) Horizontal dipole selection.

the feed current on the two input terminals (to the dipole arms) can, as expected, also be observed to have approximately 180° difference.

Fig. 10 presents photographs of a realized 2.4-GHz planar polarization-diversity antenna on an FR-4 substrate. The computed and measured VSWR are shown in Fig. 11 for both vertical and horizontal dipole selections. Satisfactory agreement between simulation and measurement is observed. The SWR is less than two from 2.2 to 3 GHz. Fig. 12 shows the computed 3-D E_θ (vertical polarization) and E_ϕ (horizontal polarization) patterns. It can be observed that the vertical or

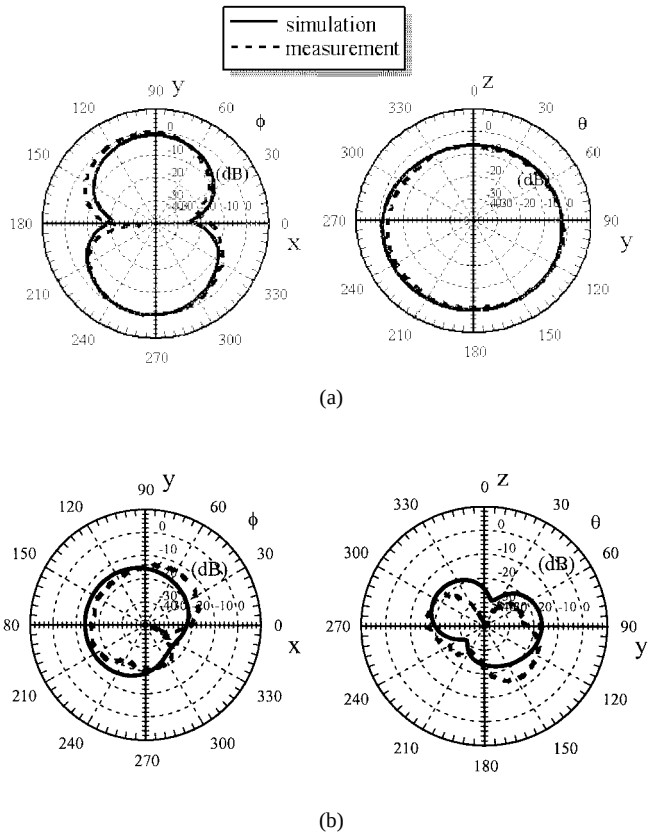

Fig. 13. 2-D radiation patterns of a 2.4-GHz polarization-diversity printed dipole antenna with vertical dipole selection. (a) Co-polarization (vertical pol): E_θ. (b) Cross-polarization (horizontal pol.): E_ϕ.

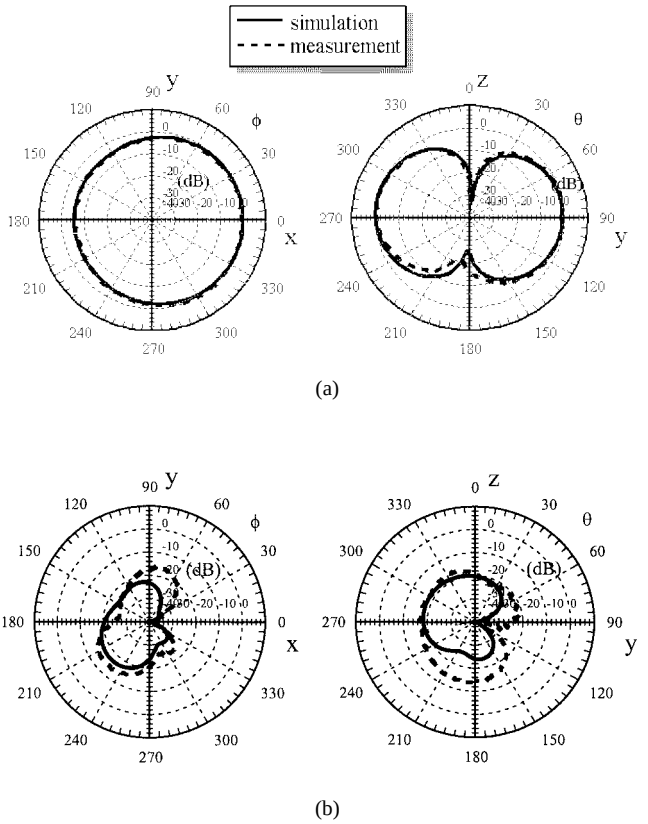

Fig. 14. 2-D radiation patterns of a 2.4-GHz polarization-diversity printed dipole antenna with horizontal dipole selection. (a) Co-polarization (horizontal pol): E_ϕ. (b) Cross-polarization (vertical pol.): E_θ.

horizontal polarization is dominant when the associated dipole section is selected. Figs. 13 and 14 show the computed and measured patterns with vertical or horizontal dipole selection at 2.45 GHz. Simulated and measured results on the co-polarization fields agree well. It can be observed that, in Fig. 13, for vertical dipole selection, the YZ-plane (H-plane) pattern is still quite omnidirectional (as an ideal vertical dipole) with some attenuation in the direction of the p-i-n-diode circuit

$$E_z^{n+1}\left(i,\,j,\,k+\frac{1}{2}\right)=\frac{1-\dfrac{\sigma\left(i,j,k+\frac{1}{2}\right)\Delta t}{2\varepsilon\left(i,j,k+\frac{1}{2}\right)}-\dfrac{\Delta z\Delta t}{2\varepsilon\left(i,j,k+\frac{1}{2}\right)R\,\Delta x\,\Delta y}}{1+\dfrac{\sigma\left(i,j,k+\frac{1}{2}\right)\Delta t}{2\varepsilon\left(i,j,k+\frac{1}{2}\right)}+\dfrac{\Delta z\,\Delta t}{2\varepsilon\left(i,j,k+\frac{1}{2}\right)R\,\Delta x\,\Delta y}}E_z^n\left(i,\,j,\,k+\frac{1}{2}\right)$$
$$+\frac{\dfrac{\Delta t}{\varepsilon\left(i,j,k+\frac{1}{2}\right)}}{1+\dfrac{\sigma\left(i,j,k+\frac{1}{2}\right)\Delta t}{2\varepsilon\left(i,j,k+\frac{1}{2}\right)}+\dfrac{\Delta z\,\Delta t}{2\varepsilon\left(i,j,k+\frac{1}{2}\right)R\,\Delta x\,\Delta y}}\left\{\begin{array}{l}\dfrac{\left[H_y^{n-1/2}\left(i+\frac{1}{2},j,k+\frac{1}{2}\right)-H_y^{n-1/2}\left(i-\frac{1}{2},j,k+\frac{1}{2}\right)\right]}{\Delta x}\\+\dfrac{\left[H_x^{n-1/2}\left(i,j-\frac{1}{2},k+\frac{1}{2}\right)-H_x^{n-1/2}\left(i,j+\frac{1}{2},k+\frac{1}{2}\right)\right]}{\Delta y}\end{array}\right\} \tag{5}$$

$$E_z^{n+1}\left(i,\,j,\,k+\frac{1}{2}\right)=\frac{1-\dfrac{\sigma\left(i,j,k+\frac{1}{2}\right)\Delta t}{2\varepsilon\left(i,j,k+\frac{1}{2}\right)}}{1+\dfrac{\sigma\left(i,j,k+\frac{1}{2}\right)\Delta t}{2\varepsilon\left(i,j,k+\frac{1}{2}\right)}}E_z^n\left(i,\,j,\,k+\frac{1}{2}\right)-\frac{\dfrac{\Delta z(\Delta t)^2}{\varepsilon\left(i,j,k+\frac{1}{2}\right)L\,\Delta x\,\Delta y}}{1+\dfrac{\sigma\left(i,j,k+\frac{1}{2}\right)\Delta t}{2\varepsilon\left(i,j,k+\frac{1}{2}\right)}}\sum_{m=1}^{n}E_z^m\left(i,\,j,\,k+\frac{1}{2}\right)$$
$$+\frac{\dfrac{\Delta t}{\varepsilon\left(i,j,k+\frac{1}{2}\right)}}{1+\dfrac{\sigma\left(i,j,k+\frac{1}{2}\right)\Delta t}{2\varepsilon\left(i,j,k+\frac{1}{2}\right)}}\left\{\begin{array}{l}\dfrac{\left[H_y^{n-1/2}\left(i+\frac{1}{2},j,k+\frac{1}{2}\right)-H_y^{n-1/2}\left(i-\frac{1}{2},j,k+\frac{1}{2}\right)\right]}{\Delta x}\\+\dfrac{\left[H_x^{n-1/2}\left(i,j-\frac{1}{2},k+\frac{1}{2}\right)-H_x^{n-1/2}\left(i,j+\frac{1}{2},k+\frac{1}{2}\right)\right]}{\Delta y}\end{array}\right\} \tag{6}$$

$$E_z^{n+1}\left(i,\,j,\,k+\frac{1}{2}\right)=\frac{1-\dfrac{\sigma\left(i,j,k+\frac{1}{2}\right)\Delta t}{2\varepsilon\left(i,j,k+\frac{1}{2}\right)}+\dfrac{C\Delta z}{\varepsilon\left(i,j,k+\frac{1}{2}\right)\Delta x\,\Delta y}}{1+\dfrac{\sigma\left(i,j,k+\frac{1}{2}\right)\Delta t}{2\varepsilon\left(i,j,k+\frac{1}{2}\right)}+\dfrac{C\Delta z}{\varepsilon\left(i,j,k+\frac{1}{2}\right)\Delta x\,\Delta y}}E_z^n\left(i,\,j,\,k+\frac{1}{2}\right)$$
$$+\frac{\dfrac{\Delta t}{\varepsilon\left(i,j,k+\frac{1}{2}\right)}}{1+\dfrac{\sigma\left(i,j,k+\frac{1}{2}\right)\Delta t}{2\varepsilon\left(i,j,k+\frac{1}{2}\right)}+\dfrac{C\Delta z}{\varepsilon\left(i,j,k+\frac{1}{2}\right)\Delta x\,\Delta y}}\left\{\begin{array}{l}\dfrac{\left[H_y^{n-1/2}\left(i+\frac{1}{2},j,k+\frac{1}{2}\right)-H_y^{n-1/2}\left(i-\frac{1}{2},j,k+\frac{1}{2}\right)\right]}{\Delta x}\\+\dfrac{\left[H_x^{n-1/2}\left(i,j-\frac{1}{2},k+\frac{1}{2}\right)-H_x^{n-1/2}\left(i,j+\frac{1}{2},k+\frac{1}{2}\right)\right]}{\Delta y}\end{array}\right\} \tag{7}$$

board. The XY-plane (E-plane) pattern is also very close to that of an ideal vertical dipole. As for the selection of the horizontal dipole (Fig. 14), similar results, which are close to those of an ideal horizontal dipole, can be seen. Also, the level of the cross-polarization field for both cases is basically less than -15 dB. The 2.4-GHz polarization-diversity antenna can be used for WLAN and wireless communication applications.

IV. Conclusion

A 2.4-GHz planar polarization-diversity printed dipole antenna with an integrated microstrip via-hole balun and polarization-switching circuit has been designed, fabricated on an FR-4 PCB board, and measured. The polarization-diversity antenna consists of two orthogonal printed dipoles for vertical and horizontal polarization and selected by a p-i-n-diode circuit. The 3-D FDTD method is used for design simulation of the complete structure of the antenna including the lumped elements in the p-i-n-diode switching circuit. The Berenger PML ABC is used for FDTD computation. The magnitude and phase of the computed surface current distribution on the top and bottom metal plates of the printed dipole antenna show the balanced current distribution due to the integrated via-hole balun. Good agreement between simulated and measured results on input VSWR and antenna patterns has been achieved. The input VSWR is approximately lower than two at 2.2∼3 GHz for either polarization selection. The antenna patterns are all close to those of an ideal vertical or horizontal dipole. The designed planar printed polarization-diversity antenna can be used for 2.4-GHz WLAN and wireless communication applications.

Acknowledgment

The authors would like to give their sincere gratitude to E. Chang and R. Liu, WavePro Inc., Taiwan, R.O.C., for the technical support of the anechoic chamber and antenna measurement system. The authors would also like to thank Prof. T.-S. Horng, Department of Electrical Engineering, National Sun-Yet Sen University, Taiwan, R.O.C., for very helpful discussion.

References

[1] K. Fujimoto and J. R. James, *Mobile Antenna Systems Handbook*. Norwood, MA: Artech House, 1994.
[2] R. P. Kronberger, H. K. Lindenmeiner, L. M. Reiter, and J. F. Hopf, "Array antenna principle applied to modern antennas for mobile communication," in *IEEE AP-S Int. Symp.*, 1998, pp. 2224–2227.
[3] J. Preiss *et al.*, "Polarization diverse antenna for portable communication devices," U.S. Patent 6 031 503, 2000.
[4] S. N. Tsai *et al.*, "Antenna module for portable computer," U.S. Patent 6 297 779, 2001.
[5] D. Edward and D. Rees, "A broadband printed dipole with integrated balun," *Microwave J.*, pp. 339–344, May 1987.
[6] N. Michishita, H. Arai, M. Nakano, T. Satoh, and T. Matsuoka, "FDTD analysis for printed dipole antenna with balun," in *Asia–Pacific Microwave Conf.*, 2000, pp. 739–742.
[7] G. S. Hilton, C. J. Railton, G. J. Ball, A. L. Hume, and M. Dean, "Finite-difference time-domain analysis of a printed dipole antenna," in *9th Int. IEEE Antennas and Propagation Conf.*, vol. 1, 1995, pp. 72–75.
[8] P. M. Melinda, A. Taflove, and J. Baron, "FD-TD modeling of digital signal propagation in 3-D circuits with passive and active loads," *IEEE Trans. Microwave Theory Tech.*, vol. 42, pp. 1514–1523, Aug. 1994.
[9] J. P. Berenger, "A perfectly matched layer for the absorption of electromagnetic waves," *J. Comput. Phys.*, vol. 114, pp. 185–200, 1994.
[10] X. Zhang and K. K. Mei, "Time-domain finite difference approach to the calculation of the frequency-dependent characteristics of microstrip discontinuities," *IEEE Trans. Microwave Theory Tech.*, vol. 36, pp. 1775–1787, Dec. 1988.
[11] J. Fang and J. Ren, "A locally conformed finite-difference time-domain algorithm of modeling arbitrary shape planar metal strips," *IEEE Trans. Microwave Theory Tech.*, vol. 41, pp. 830–838, May 1997.
[12] D. Koh, H.-B. Lee, and T. Itoh, "A hybrid full-wave analysis of via-hole grounds using finite-difference and finite-element time-domain methods," *IEEE Trans. Microwave Theory Tech.*, vol. 45, pp. 2217–2223, Dec. 1997.
[13] A. Taflove, Ed., *Advances in Computational Electrodynamics the Finite-Difference Time Domain Method*. Norwood, MA: Artech House, 1996.
[14] D. M. Pozar, *Microwave Engineering*. New York: Wiley, 1998, p. 576.

Huey-Ru Chuang (M'88) received the B.S.E.E. and M.S.E.E. degrees from the National Taiwan University, Taipei, Taiwan, R.O.C., in 1977 and 1980, respectively, and Ph.D. degree in electrical engineering from Michigan State University, East Lansing, in 1987.

From 1987 to 1988, he was a Post-Doctoral Research Associate with the Engineering Research Center, Michigan State University. From 1988 to 1990, he was with the Portable Communication Division, Motorola Inc., Ft. Lauderdale, FL. In 1991, he joined the Department of Electrical Engineering, National Cheng Kung University, Tainan, Taiwan, R.O.C., where he is a Professor. His research interests include portable antenna design, RF/microwave circuits, and RF integrated circuits (RFICs)/monolithic microwave integrated circuits (MMICs) for wireless communications, electromagnetic computation of the human interaction with mobile antennas, electromagnetic interference (EMI)/electromagnetic compatibility (EMC), microwave communication, and detection systems.

Liang-Chen Kuo (S'98) received the B.S.E.E. degree from the Nan-Tai Institute of Technology, Tainan, Taiwan, R.O.C., in 1987, the M.S.E.E. degree from the Tatung Institute of Technology, Taipei, Taiwan, R.O.C., in 1996, and is currently working toward the Ph.D. degree in electrical engineering at the National Cheng Kung University, Tainan, Taiwan, R.O.C.

His research interests include computational electromagnetics and antenna design.